Materials Horizons

ROYAL SOCIETY OF CHEMISTRY

COMMUNICATION

Published on 02 July 2026

Cite this: DOI: 10.1039/d6mh00984k

Received 15th May 2026,
Accepted 29th June 2026

DOI: 10.1039/d6mh00984k

rsc.li/materials-horizons

Development of high-performance NIR-to-SWIR down-shifting $Li_3Ba_2Gd_3(MoO_4)_8$:Yb^{3+}/Tm^{3+} and Yb^{3+}/Ho^{3+} for phosphor conversion LEDs

Krishnan Rajagopalan,*[a] Yang Lu,[a] Eduard Madirov,[a] Bryce S. Richards *[ab] and Andrey Turshatov *[a]

High-performance short-wave infrared (SWIR) phosphors are of increasing interest for phosphor-converted light-emitting diodes (pc-LEDs) used in sensing, imaging, and analytical applications. In this work, $Li_3Ba_2Gd_3(MoO_4)_8$ (LBGMO) phosphors co-doped with Yb^{3+}/Tm^{3+} and Yb^{3+}/Ho^{3+} were developed as efficient near-infrared (NIR)-to-SWIR down-shifting (DS) materials. Phase purity and crystal structure were confirmed by X-ray diffraction, demonstrating successful incorporation of rare-earth ions into the LBGMO host lattice. Under 940 nm excitation, efficient sensitization by Yb^{3+} ions enables strong SWIR emission from both activator ions. The Yb^{3+}/Tm^{3+} system exhibits broadband emission centered at approximately 1800 nm, originating from the Tm^{3+}: $^3F_4 \rightarrow {}^3H_6$ transition, whereas the Yb^{3+}/Ho^{3+} system shows dominant emission near 2050 nm associated with the Ho^{3+}: $^5I_7 \rightarrow {}^5I_8$ transition. High photoluminescence quantum yields (PLQY) of 63% and 69% were achieved for the Yb^{3+}/Tm^{3+} and Yb^{3+}/Ho^{3+} phosphors, respectively, accompanied by efficient energy transfer from Yb^{3+} to Tm^{3+} (95%) and Ho^{3+} (96%). The moderate cut-off phonon energy of 930 cm^{-1} supports efficient population of the lower-energy SWIR-emitting states, while the rate of non-radiative relaxation remains sufficiently low to prevent effective competition with radiative transitions. Phosphor-converted LED devices using 940 nm excitation and fabricated with the developed phosphor conversion layers exhibited maximum wall-plug efficiencies of 1.6% for Yb^{3+}/Tm^{3+} and 3.6% for Yb^{3+}/Ho^{3+}. Demonstration of SWIR imaging through visibly opaque materials and spectral overlap with water absorption bands confirms the potential application of these materials.

New concepts

Current phosphor-converted SWIR light sources are mainly limited by low conversion efficiency, restricted spectral tunability, and poor compatibility with low-cost excitation sources. In this work, we introduce $Li_3Ba_2Gd_3(MoO_4)_8$ co-doped with Yb^{3+}/Tm^{3+} and Yb^{3+}/Ho^{3+} as an efficient material platform for NIR-to-SWIR down-shifting under technologically relevant 940 nm excitation. The developed phosphors exhibit broadband emission in the 1700–2100 nm spectral range together with high photoluminescence quantum yields reaching 63% and 69%, enabled by highly efficient Yb^{3+}-sensitized energy transfer and favorable host-lattice phonon properties. In addition to spectroscopic investigation, practical phosphor-converted SWIR LED devices were demonstrated with wall-plug efficiencies up to 3.6%. The work further demonstrates SWIR imaging through visibly opaque materials and spectral overlap with water absorption bands, highlighting application potential in sensing and analytical imaging.

1. Introduction

The classification of the spectral region between 780 and 3000 nm is not universally standardized and varies across different research fields. For example, in imaging spectroscopy and remote sensing, short-wave infrared (SWIR) light is commonly defined as the 1000–2500 nm spectral range, representing the long-wavelength portion of the near-infrared (NIR) region.[1,2] In contrast, the international standard ISO 20473 classifies this wavelength range into IR-A (780–1400 nm) and IR-B (1400–3000 nm).[3] Furthermore, biomedical imaging frequently employs a different nomenclature, distinguishing NIR-I (700–900 nm), NIR-II (1000–1700 nm), and NIR-III (2080–2340 nm) spectral windows.[4] In the present work, the investigated wavelength range is referred to as the SWIR region following the convention widely adopted in imaging spectroscopy and remote-sensing applications. SWIR offers reduced scattering, deeper penetration through complex media (especially biological), improved imaging contrast, and eye-safe operation compared to visible and shorter NIR wavelengths,[5–7] making it uniquely suited for advanced imaging and sensing applications.[8,9] Free-space optical communication systems prefer wavelengths near 1550 nm, allowing higher

[a] Institute of Microstructure Technology, Karlsruhe Institute of Technology, Hermann-von-Helmholtz-Platz 1, 76344, Eggenstein-Leopoldshafen, Germany. E-mail: krishnan.rajagopalan@kit.edu, bryce.richards@kit.edu, andrey.turshatov@kit.edu

[b] Light Technology Institute, Karlsruhe Institute of Technology, Engesserstraße 13, 76131, Karlsruhe, Germany

pulse energies despite water vapor absorption due to low attenuation, while lidar technologies use longer SWIR wavelengths to achieve extended detection range with minimal retinal hazard.[10–12] SWIR illumination enables optical sorting devices to efficiently identify polymers in a waste stream *via* absorption in the 1000–1600 nm range.[13] SWIR light near 1400 or 1940 nm allows non-contact, real-time monitoring of water content by probing O–H vibration bands in food processing, medicines, and industrial quality control.[14,15] The SWIR region contains characteristic absorption features of hydroxyl (O–H) and C–H groups, enabling mineral identification, hyperspectral mapping, spectroscopy, and environmental monitoring, thereby driving demand for compact SWIR light sources.[16] These advantages have driven intense interest in developing compact, efficient, and spectrally-tunable SWIR light sources suitable for portable and integrated devices.

Quartz–tungsten–halogen (QTH) lamps,[17] gas-discharge lamps,[17] GaSb-laser diodes,[17] Tm^{3+}-fiber lasers,[17] optical parametric oscillators,[17] and superluminescent diodes (SLD)[17] emit broadband or high-power SWIR light but have low efficiency, short life time, high thermal load, limited spectral coverage, complex device architectures, strict operating requirements, or high cost.[17] Despite advances in semiconductor-based SWIR LEDs, many products struggle to emit strongly in the 1500–2200 nm region. The AlGaAs, InGaAsP, and InP family of III–V materials is often used to achieve SWIR emission in this wavelength range.[18] However, the major concerns, such as complex heterostructures, bandgap engineering, formation of dislocations and crystalline defects, and insertion of buffer layer, can potentially limit progress toward powerful light sources for next-generation photonic applications.[19–21] Hence, it is necessary to find new SWIR-emitting materials and new strategies, such as phosphor-conversion LEDs (pc-LEDs).

In pc-LEDs, a primary LED stimulates phosphor material, which re-emits at longer wavelengths. When built with appropriate phosphors, pc-LEDs combine broadband emission, compact form factor, mechanical resilience, and simple electrical driving units.[9,22–24] Compared with QTH lamps, SLDs and LEDs, SWIR pc-LEDs (for instance Ni^{2+}-based[31]) offer advantages including low cost, high efficiency, durability, large bandwidth, high contrast ratio, portability, and spectral tunability. These properties make SWIR pc-LEDs particularly promising for applications requiring compact, robust, and spectrally-versatile illumination. Comparative performance characteristics of the aforementioned SWIR light sources are given in Table S1, whereas Fig. 1 displays the relative spectral emission characteristics of common SWIR light sources, illustrating trade-offs between bandwidth, emission range, and their approximate wall-plug efficiency (WPE).

Trivalent rare-earth (RE^{3+})-doped inorganic phosphors offer significant advantages for pc-LEDs, including high chemical stability, broadband yet tunable emission, high quantum yield, and excellent compatibility with existing device architectures.[33–35] In particular, excitation in the 940–980 nm range can be efficiently achieved *via* ytterbium (Yb^{3+})-based sensitization. Yb^{3+} is widely employed as a sensitizer due to its simple two-level energy scheme ($^2F_{7/2} \leftrightarrow {}^2F_{5/2}$) and strong absorption in the ≈900–1000 nm region. Moreover, Yb^{3+} can efficiently transfer excitation energy to neighboring RE activators such as: (i) erbium (Er^{3+}), which typically exhibits emission around ∼1500 nm[36]; (ii) Tm^{3+}, which, depending on the host lattice and dopant concentration, exhibits emission centered at ∼1800 nm ($^3H_4 \rightarrow {}^3F_6$); and (iii) holmium ($Ho^{3+}$) that exhibits characteristic emission near ∼2100 nm ($^5I_7 \rightarrow {}^5I_8$). Collectively, these three activators provide coverage across a broad spectral range, spanning approximately 1500–2200 nm.

To date, co-doped phosphors containing Tm^{3+} and Ho^{3+} have been shown to exhibit 1500–2200 nm SWIR emission in both glass[37,38] and single-crystal hosts.[39–42] However, reports on micron-scale, RE co-doped powder phosphors operating in the extended SWIR range (particularly 1500–2200 nm) remain relatively scarce. Therefore, systematic studies to optimize RE^{3+} dopant concentrations, elucidate energy-transfer mechanisms, and quantify photoluminescence quantum yields (PLQY) across

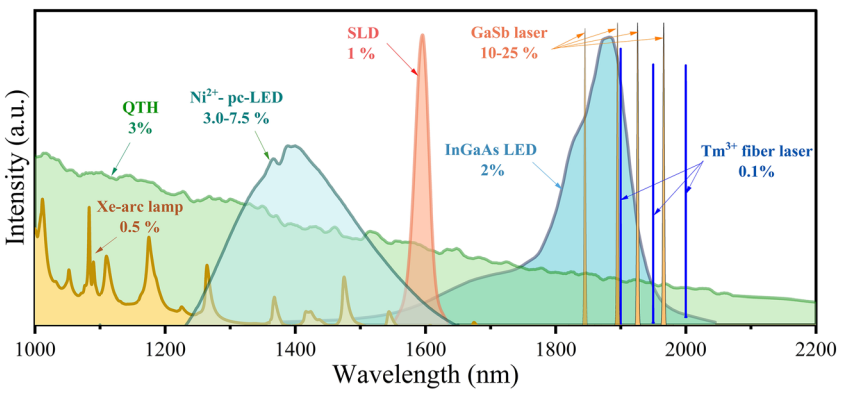

Fig. 1 Representative spectral output of common continuous SWIR light sources in the wavelength range of 1000–2200 nm. The figure highlights the fundamentally different spectral characteristics of various SWIR-emitting sources and compares their wall-plug efficiency (WPE) – sometimes called radiant efficiency – which describes the fraction of electrical power converted into optical output. Emission profiles are shown for of a QTH lamp (T = 3000 K, 1000–2200 nm) with WPE of 3%,[25] xenon arc lamp (1000–2200 nm) with WPE of 0.5%,[26,27] Ni^{2+} based pc-LED (1250–1650 nm) with WPE of 3.0 – 7.5%,[28] SLD (1550–1630 nm) with WPE of 1%,[29] InGaAs LED (∼1800–2000 nm) with WPE of 2%,[30] GaSb-based laser diodes (1870 nm, 1908 nm, 1940 nm, 1980 nm) with WPE of ∼10–25%,[31] Tm^{3+}-doped fiber laser (1900 nm, 1950 nm and 2000 nm) with WPE of ∼0.1%.[32]

the 1500–2200 nm range are urgently needed to address this gap. Ideal host materials for high-performance NIR phosphors should exhibit a wide optical bandgap to suppress carrier excitation into the conduction band, a high radiative recombination rate, and suitable phonon energies to minimize multiphonon relaxation while enabling phonon-assisted energy transfer, thereby enhancing PLQY. In addition, chemical and thermal robustness is required for device integration, along with crystallographic sites that can accommodate multiple rare-earth ions while minimizing clustering and concentration quenching. In this context, oxide-based powder hosts offer excellent chemical and thermal stability, compatibility with established solid-state synthesis routes, and strong potential for scalable device integration.

Double molybdates, in particular, have emerged as promising hosts. Their frameworks often combine moderate phonon energies with structural flexibility and multiple cation sites, which facilitate energy migration among RE^{3+} ions.[43] Moreover, in double molybdates, the presence of RE^{3+} ions can promote energy-migration networks that facilitate long-range energy transfer from the sensitizer to the activator. A recent study reported that Yb^{3+}/Er^{3+}-doped $Li_3Ba_2Gd_3(MoO_4)_8$ (LBGMO) exhibits SWIR emission at 1540 nm with a PLQY of ~70%.[43] The structural tolerance of the LBGMO lattice enables the incorporation of multiple RE^{3+} ions at Gd^{3+} sites with comparable ionic radii, promoting a homogeneous dopant distribution while suppressing excessive clustering and concentration quenching. Moreover, the LBGMO framework provides a suitable environment for rare-earth dopants, facilitating long-range sensitizer–activator energy transfer, as demonstrated for Yb^{3+}/Er^{3+}-doped systems. Collectively, these attributes establish LBGMO as a promising platform for exploring Yb^{3+}-sensitized Tm^{3+} and Ho^{3+} emission in the extended SWIR region.

In this work, the synthesis, structural characterization, and comprehensive spectroscopic investigation of LBGMO doped with Yb^{3+} and co-doped with either Tm^{3+} or Ho^{3+} is reported. The site occupancy and phase purity are systematically examined, along with steady-state and time-resolved photoluminescence (PL), excitation pathways, and energy-transfer dynamics. By directly comparing $Yb^{3+} \rightarrow Tm^{3+}$ and $Yb^{3+} \rightarrow Ho^{3+}$ sensitization within the same LGBMO host, it is elucidated how the choice of activator governs emission bandwidth, peak position, optimal PLQY, and thermal quenching behaviour. These findings establish key design principles for high-performance Yb^{3+}-sensitized NIR phosphors and demonstrate the potential of LBGMO as a versatile platform for broadband SWIR pc-LED and sensing applications.

2. Experimental section

2.1 Solid-state synthesis of LBGMO:Yb^{3+}/Tm^{3+} and Yb^{3+}/Ho^{3+} phosphors

$Li_3Ba_2Gd_{(3-x-y)}Yb_xTm_y(MoO_4)_8$ (LBGMO:Yb^{3+}/Tm^{3+}) or $Li_3Ba_2Gd_{(3-x-y)}Yb_xHo_y(MoO_4)_8$ (LBGMO:Yb^{3+}/Ho^{3+}) phosphors were synthesized *via* a conventional high-temperature solid-state reaction. Analytical-grade Li_2CO_3, $BaCO_3$, Gd_2O_3, MoO_3, Yb_2O_3, and Tm_2O_3 (or Ho_2O_3) powders (≥99.9%, chemPUR) were used as starting precursors without any further purification. Stoichiometric amounts of the precursors, corresponding to the nominal compositions of x = 0.2–2.7 and y = 0.1–0.4 were accurately weighed and homogenized by thorough grinding in an agate mortar for 30 min. The homogeneous mixtures were transferred into covered alumina crucibles and annealed in air. The heating profile consisted of direct annealing to 900 °C at 5 °C min^{-1} and 3 h of annealing in a programmable furnace (KLS-05/1, Thermconcept). After natural cooling to room temperature, the products were crushed and reground to obtain micron-sized phosphor powders for subsequent characterization.

Luminescent down-shifting (LDS) spectra and PLQY were investigated for systematic variation in dopant concentration. First, the Tm^{3+} (or Ho^{3+}) content was fixed at y = 0.1, while the Yb^{3+} concentration was varied (x = 0.2 to 2.7). In a complementary series, Yb^{3+} was fixed after the first optimization, and the concentration of activator ions (Tm^{3+} or Ho^{3+}) was varied (y = 0.2 to 0.4). The obtained powders were stored in sealed plastic cuvettes under dry conditions prior to structural and spectroscopic characterization.

2.2 Structural and morphological characterization

The crystal structure of the as-prepared LBGMO:Yb^{3+}/Tm^{3+} and LBGMO:Yb^{3+}/Ho^{3+} powders was examined by X-ray diffraction (XRD) using a diffractometer (D2 Phaser, Bruker) over a 2θ range of 10–70°. Rietveld refinements of the powder XRD patterns were performed using the TOPAS software package. Particle morphology and size distribution were investigated using a scanning electron microscope (SEM) equipped with an SE-II detector (SUPRA 60VP, Zeiss). To improve imaging contrast, the samples were coated with a thin silver layer prior to analysis. A laser particle size analyzer (Analysette 22 NeXT Nano, Fritsch) was used to determine the particle size distribution (measurement range 0.01 to 3800 μm). Q3 (cumulative) and dQ3 (differential) correspond to particle size distribution, denoting the cumulative % of particles (by volume) and differential % of particles within a small size interval (by volume), respectively.

2.3 Optical characterization

Diffuse reflectance spectra (DRS) in the NIR range were recorded using a spectrophotometer (Cary 7000, Agilent) equipped with an integrating sphere in the reflectance mode. The PLQY and LDS spectra were measured in a custom-built optical system.[44] The sample was placed in an integrating sphere (∅ 6″, 3P-LPM-060-SL, Labsphere) and excited with a laser diode operating at 976 nm (RLT980-200GS, Roithner). The excitation source was mounted on a temperature-controlled mount (TCLDM9, Thorlabs) and driven by a diode laser controller (ITC4001, Thorlabs). The emission was detected using a SWIR spectrometer (PGS NIR 2.2, Zeiss). To eliminate the scattered excitation radiation, a 980 nm long-pass filter (LP02-980RE-25, Semrock) was placed between the integrating sphere output and the collecting fiber (BFY200MS02, Thorlabs). The entire system is automated and controlled using custom software developed using the LabVIEW environment. The PLQY was calculated using the 3M approach.[45] Laser power and beam profiling were carefully monitored.

A quartz wedge reflected a portion of the excitation beam onto a calibrated silicon photodiode (S121C, Thorlabs) connected to a power meter (PM320E, Thorlabs). Beam dimensions were determined with a beam profiler (BP209-IR/M, Thorlabs) using the 2σ criterion. For the 976 nm laser, the beam area was 57.4×10^{-3} cm^2, yielding the excitation power density of 0.67 W cm^{-2}. Low power density mode was chosen to minimize the heating as well as any upconversion emission from the sample. A 3–5% uncertainty in PLQY was assumed for all measurements, based on earlier work that thoroughly evaluated the repeatability of the measurements.[46] We used an in-house optical system with an infrared single-photon detector (ID Quantique, ID220) connected to a multi-channel scale card (TimeHarp 260, Picoquant) to measure the LDS decay time. The temperature-dependent luminescence properties were investigated utilizing a custom-built setup equipped with a high-performance temperature control stage (Microptik BV, MTDC600). The sample was exposed to irradiation with a 940 nm laser (Thorlabs, M9-940-0200) and was heated at a rate of 0.5 K s^{-1}, and its luminescence was measured using an NIR spectrometer (Ocean Insight, NIRQuest). Upconversion (UC) spectra and UCPLQY were measured using a custom-built optical setup based around an integrating sphere (Labsphere, ∅15 cm, 3P-LPM-060-SL) and a CCD spectrometer (Avantes, AvaSpec-ULS2048 × 64TEC). The setup was calibrated using a calibration lamp (Ocean Optics, HL-3plus-INT-CAL-EXT). The samples were excited using a 980 nm continuous-wave (CW) laser diode (Thorlabs, L980P200).

2.4 Coating, device fabrication and operation

The phosphors LBGMO:Yb^{3+}/Tm^{3+} or LBGMO:Yb^{3+}/Ho^{3+} were mixed (70 wt% phosphor powder) with a two-part addition-cure silicone resin (RTV615, Momentive Performance Materials) for device fabrication. For a total batch mass of 2.0 g, 0.40 g of phosphor was mixed with 1.60 g of silicone (Part A : Part B = 10 : 1 by weight). The phosphor was first homogenized in Part A, followed by the addition of Part B and thorough mixing. The resulting mixture was degassed in a vacuum oven (Thermo-Scientific, VT 6060 M, Thermo Electron LED GmbH) and directly deposited onto a 940 nm LED chip (ILH-IS01-94SN-SC201-WIR200, RS Photonics), resulting in LED940@Tm and LED940@Ho chips. Alternatively, a 980 nm InGaAs LED chip (SMB1N-980D, Roithner) was also coated with a similar silicon resin layer, resulting in LED980@Tm and LED980@Ho chips. However, the concentration of phosphors in the silicon resin was reduced to 20 wt% in the case of 980 nm chip. The coated chip was subsequently degassed again under vacuum to remove residual air bubbles and cured at 60 °C for 3 h to yield a uniform conversion layer. The device was then mounted on an aluminum heat sink. The LED chips were operated under forward-bias conditions using a regulated DC power supply in constant-current mode. The driving current was varied from 50 to 300 mA for the 940 nm chip and from 50 to 600 mA for the 980 nm chip to evaluate device performance, while the forward voltage and input power were monitored simultaneously. The emission intensity of the SWIR pc-LEDs was estimated by placing an LED at the port of an integrating sphere (Labsphere, 6 in. ∅, 3 P-LPM-060-SL) and obtaining spectra using a calibrated SWIR spectrometer (Zeiss PGS NIR 2.2). This provided the number of photons per cm^2 of area and per nm of the spectral range at various drive currents. The spectra were integrated within the 900–1200 nm range for the LED without a spectral conversion layer, the 1500–2200 nm range for the LED with a Yb^{3+}/Tm^{3+} conversion layer, and the 1500–2400 nm range for the LED with a Yb^{3+}/Ho^{3+} conversion layer, eventually yielding the optical emission power. The wall-plug efficiency was calculated as the ratio of the optical emission power to the diode's electric power. This was estimated as the product of the applied voltage and current. The images in the visible spectral range were taken with a phone camera (Apple iPhone 13). Thermal images of the LEDs were taken with a thermal camera (FLIR ONE PRO, Teledyne FLIR LLC).

Hyperspectral imaging of sunflower seeds was performed as follows: all images were acquired using a SWIR hyperspectral camera (FX17, Specim). The samples were placed on a Specim LabScanner scanner 30 cm away from the camera optics and illuminated using an LED with a SWIR conversion layer. The samples were scanned at a rate of 4 mm s^{-1} with an integration time of 50 ms. The acquired data were processed using custom software. In the case of the LED with a Yb^{3+}/Tm^{3+} conversion layer, the quasi-RGB image was built as follows: the spectra in each pixel were integrated into the 1100–1300 nm, 1500–2200 nm and 2300–2500 nm ranges, providing the intensities in the "blue, green and red" channels, respectively. In the case of the LED with Yb^{3+}/Ho^{3+} conversion layer, the quasi-RGB image was built using the integrated intensities in the 1100–1300 nm, 1500–1980 nm and 1981–2400 nm as "blue, green and red" channels respectively. The SWIR images shown in color (Fig. 6 and 8) are false-color renderings generated by the hyperspectral SWIR camera to visualize the detected SWIR intensity, as SWIR radiation is not visible to the human eye.

In the case of the LED with Yb^{3+}/Ho^{3+} conversion layer, identification of the dry and wet samples was performed as follows: in each pixel, the spectra were integrated into two ranges: 1500–1980 nm and 1981–2400 nm. Then, the ratio of these two intensities was estimated. Pixels with a ratio higher than the threshold value of 0.5 were identified as dry, and pixels with a ratio lower than the threshold value were identified as wet. Pixels where the integrated intensity of both ranges was lower than a set value were designated as dark. The representative spectra are taken from the pixels with the highest and lowest intensity ratio values.

3. Results and discussion

3.1 Structural and morphological characterization

Powder XRD patterns of the synthesized LBGMO:Yb^{3+}/Tm^{3+} and LBGMO:Yb^{3+}/Ho^{3+} phosphors were collected to verify phase purity and examine the influence of RE^{3+} substitution on the crystal structure. Fig. 2a and Fig. 2b demonstrate the XRD patterns of LBGMO co-doped with Yb^{3+}/Tm^{3+} and Yb^{3+}/Ho^{3+} ions, respectively. Within this series of samples, the

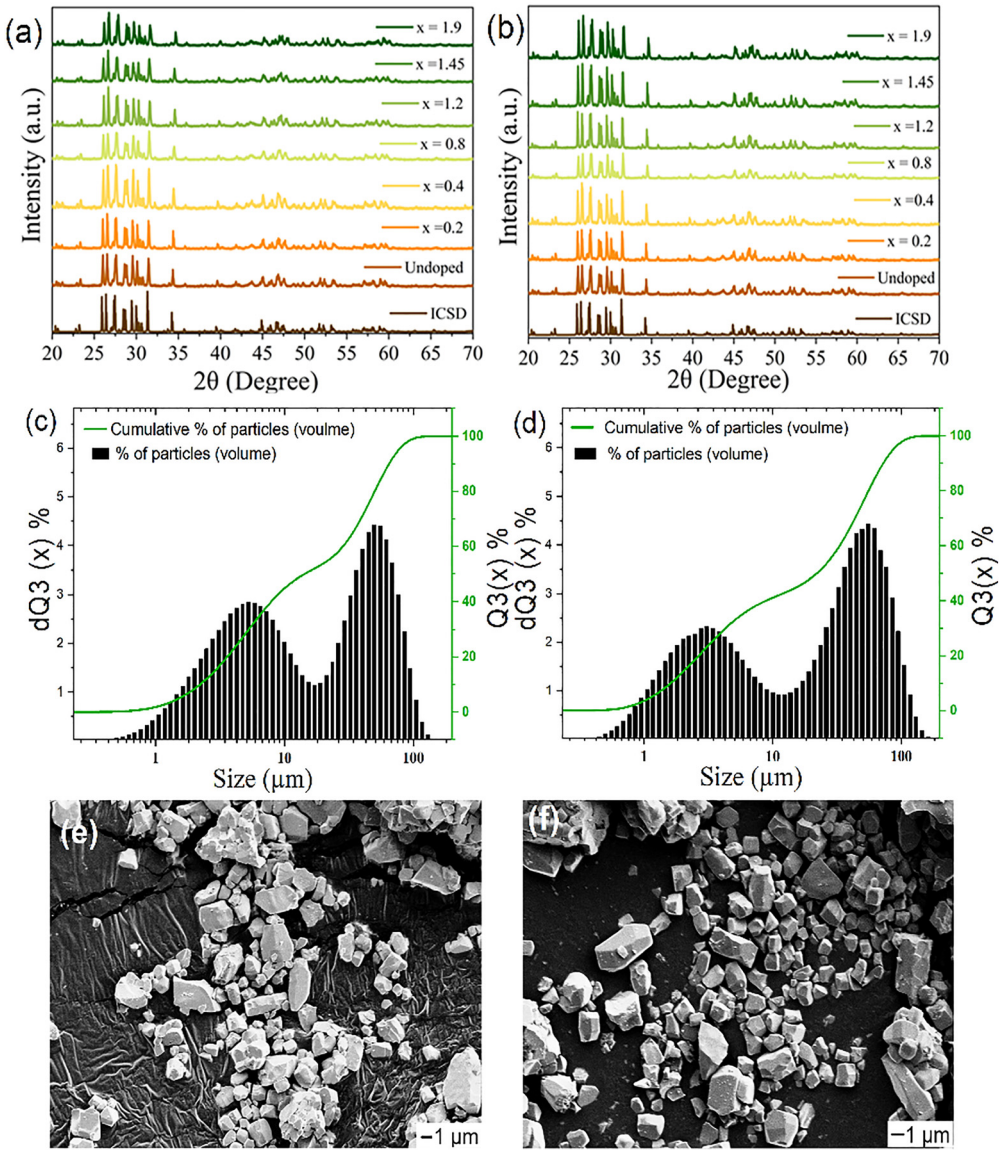

Fig. 2 (a) Powder XRD patterns of LBGMO doped with various Yb^{3+}(x) doping concentrations (x = 0.2, 0.4, 0.8, 1.2, 1.45, 1.9) while maintaining fixed concentration of (a) y = 0.1 Tm^{3+}, (b) 0.1 Ho^{3+}. (c) and (d) Particle size distribution histogram images of representative LBGMO phosphors co-doped with Yb^{3+}/Tm^{3+} (x = 0.8; y = 0.1), Yb^{3+}/Ho^{3+} (x = 2.7; y = 0.1), respectively. The corresponding SEM images are presented in (e) and (f).

concentrations of Tm^{3+} or Ho^{3+} are fixed (y = 0.1), while the Yb^{3+} concentration was varied (x = 0.2 to 1.9 for the series Yb^{3+}/Tm^{3+} and x = 0.2 to 2.7 for the series Yb^{3+}/Ho^{3+}). All the reflections can be indexed as corresponding to the monoclinic $C2/c$ phase typical of the LBGMO family (ICSD-39580), confirming that the host lattice is retained upon co-doping with Yb^{3+}/Tm^{3+} and Yb^{3+}/Ho^{3+}. This result indicates complete incorporation of the dopant ions into the Gd^{3+} sublattice. Rietveld refinement results for representative compositions are presented in Fig. S1(a–c), to check the crystalline phase purity and successful incorporation of the dopant ions into the host lattice. The refined lattice parameters obtained from the Rietveld refinement are summarized in Table S2. A weak reflections at $2\theta \approx 21.21^\circ$ and 43.47° appears in all undoped and doped LBGMO samples (Fig. S1a) whose position and intensity remain unchanged with varying Yb^{3+}/Tm^{3+} and Yb^{3+}/Ho^{3+} concentrations (Fig. S1b and c). These minor impurity peaks are attributed to a trace secondary phase formed during synthesis. With increasing Yb^{3+} concentration another, a weak reflection is observed at $2\theta \approx 24.89^\circ$, (Fig. S1c) due to local structural distortions associated with the higher Yb^{3+} doping content (x = 2.7) suggesting the possible formation of a minute secondary phase. In addition, the all strongest diffraction peak in the range of 2θ: 24–38° shift gradually toward higher 2θ values with increasing x (Fig. S2 and S3), reflecting a contraction of the unit cell due to the smaller ionic radius of Yb^{3+} (0.985 Å, CN = 8), Tm^{3+} (0.994 Å, CN = 8) and Ho^{3+} (1.015 Å, CN = 8) compared to Gd^{3+} (1.053 Å).[47] The unit-cell volume decreases from 1285.96 $Å^3$ for undoped LBGMO to 1273.15 $Å^3$ for LBGMO:0.80Yb^{3+}/0.10Tm^{3+} and further to 1247.60 $Å^3$ for LBGMO:2.7Yb^{3+}/0.10Ho^{3+} (Table S2). Such behavior is consistent

with analogous peak shifts reported for Yb^{3+}/Er^{3+} substitution in LBGMO,[43] confirming that the observed trend serves as a sensitive indicator of successful incorporation at the rare-earth sites.

When the Yb^{3+} concentration was fixed at its optimized value, the activator ion concentrations (Tm^{3+} or Ho^{3+}) were systematically varied within the range $y = 0.1$–0.4. No considerable changes were observed in the XRD patterns after increasing the activator concentrations, confirming that all doped specimens retain the single-phase monoclinic structure of the LBGMO host. The corresponding XRD profiles for the concentration series are provided in Fig. S4 and S5.

This structural stability is expected to support a homogeneous dopant distribution and well-defined interionic distances, thereby sustaining efficient energy-transfer pathways between Yb^{3+} and the activator ions (Tm^{3+} or Ho^{3+}) under optical excitation. As described above, the crystal framework consists of isolated MoO_4^{2-} tetrahedra interconnected *via* Ba^{2+} and Li^{+} cations, while RE^{3+} ions occupy two nonequivalent coordination sites within the monoclinic lattice. The ability of this host to accommodate high concentrations of RE^{3+} ions without a change in symmetry arises from its flexible polyanionic network and the tolerance of the Ln–O polyhedra to local distortion.[48]

In addition to the XRD results, the particle size distribution obtained using static light scattering (Fig. 2(c and d)) reveals a bimodal profile, indicating the presence of two distinct particle populations with an average size of ∼50 μm and an overall size range spanning 1–100 μm. SEM analysis (Fig. 2(e and f)) further confirms the presence of agglomerated microcrystalline clusters with polygonal morphology and a broad size distribution. Notably, the particle size and morphology remain largely unaffected by Yb^{3+}/Tm^{3+} and Yb^{3+}/Ho^{3+} doping.

3.2 Optical properties of LBGMO:Yb^{3+}/Tm^{3+}

Fig. 3a displays the DRS (green line), featuring several well-defined absorption bands in the NIR region that are attributed to characteristic 4f–4f transitions of Yb^{3+} and Tm^{3+} ions. Owing to its wide bandgap (E_g − 3.65) eV,[48] the LBGMO host remains optically transparent across the NIR/SWIR range. This suppresses host-related absorption and ensures that excitation and emission processes are primarily localized on the RE^{3+} ions. The broad absorption band in the range of 920–1020 nm (centered at ∼975–985 nm) corresponds to the Yb^{3+}: $^2F_{7/2} \rightarrow {}^2F_{5/2}$ transition, confirming efficient spectral overlap with the 940 nm or 980 nm excitation of the LED chips. Additional absorption bands observed near ∼1200 and ∼1700 nm are assigned to Tm^{3+}: $^3H_6 \rightarrow {}^3H_5$ and Tm^{3+}: $^3H_6 \rightarrow {}^3F_4$ transitions. Notably, Tm^{3+} does not exhibit significant absorption at 980 nm, indicating that efficient $Yb^{3+} \rightarrow Tm^{3+}$ energy transfer is essential to achieve strong SWIR emission.

Upon 980 nm excitation, the LDS spectrum (black line) presented in Fig. 3a displays two prominent emission bands centered at approximately ∼1020 nm and ∼1800 nm. The emission near 1020 nm arises from the Yb^{3+}: $^2F_{5/2} \rightarrow {}^2F_{7/2}$ transition, representing direct radiative relaxation of the sensitizer. The broad and intense band spanning 1650–1950 nm is attributed to the Tm^{3+}: $^3F_4 \rightarrow {}^3H_6$ transition, which constitutes the principal LDS emission channel. The observation of Tm^{3+} NIR emission under 980 nm excitation indicates the occurrence of non-radiative energy transfer from Yb^{3+} sensitizers to Tm^{3+} activators. This transfer is mediated by a phonon-assisted mechanism within the Förster framework,[49] which was modeled so far only by using Dexter's phonon-assisted energy transfer (PAET) formalism.[50] It should be clarified that this process is not refered to a phonon-assisted upconversion back energy transfer energy-transfer process ($Yb^{3+} \rightarrow Tm^{3+}/Ho^{3+}$), which can occur at elevated temperatures and typically requires the absorption of multiple phonons.[51] Instead, we referred to the downshifting energy-transfer process from Yb^{3+} to Tm^{3+}/Ho^{3+} ions following excitation of the Yb^{3+}: $^2F_{7/2} \rightarrow {}^2F_{5/2}$ transition at 980 nm. The energy level diagram in Fig. 3b summarizes the relevant ground- and excited-state transitions of Yb^{3+} and Tm^{3+} ions (including possible UC phenomena Fig. S6). Under 980 nm excitation, sensitization of Tm^{3+} emission proceeds *via* Yb^{3+} absorption, where a photon excites Yb^{3+} to the $^2F_{5/2}$ excited state. Subsequent phonon-assisted energy transfer populates the $^3H_5$ level of Tm^{3+}. This level rapidly relaxes non-radiatively to the lower-lying $^3F_4$ state *via* multiphonon processes. Finally, radiative relaxation from the $^3F_4$ level to the $^3H_6$ ground state

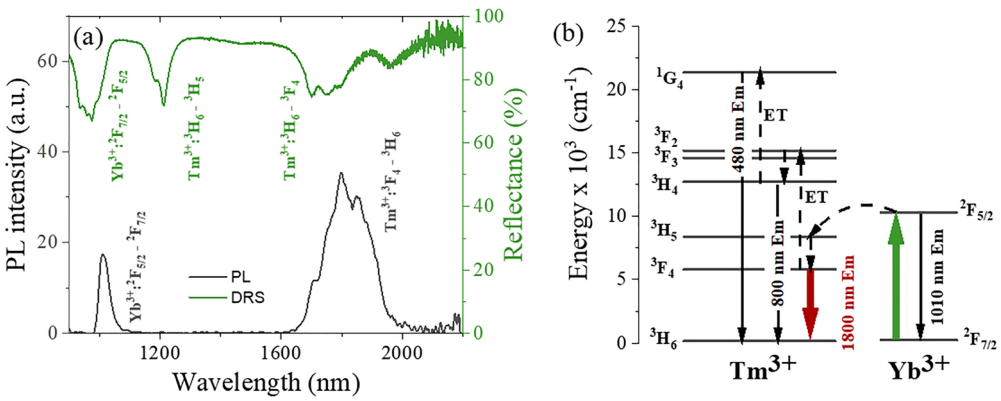

Fig. 3 (a) Representative DRS and LDS spectrum upon 980 nm excitation of the LBGMO:Yb^{3+}/Tm^{3+} phosphor ($x = 0.8$; $y = 0.1$); (b) energy level diagram of the Tm^{3+} and Yb^{3+} ions, solid and dashed lines display radiative and non-radiative processes, respectively.

gives rise to emission centered at ~1800 nm. The full-width at half-maximum (FWHM) of the 1800 nm emission exceeds 160 nm, indicating a broad emission suitable for broadband NIR sources in spectroscopy and imaging. Such broadband emission arises from the crystal-field splitting of the $^3F_4$ and $^3H_6$ states of Tm^{3+} in the low-symmetry Gd^{3+} sites of the LBGMO lattice.[52] The high intensity and broad bandwidth together demonstrate that this material can act as an efficient Yb^{3+}-sensitized Tm^{3+} emitter for NIR photonic applications.

To further investigate the luminescence in the LBGMO:Yb^{3+},Tm^{3+} phosphors, two series of samples were examined. The first one had the Tm^{3+} doping fixed at $y = 0.1$ and Yb^{3+} doping varied from $x = 0.2$ to 2.5 (Fig. 4a). All samples exhibit the same characteristic emission bands. The emission intensity increases as the dopant concentration is raised from 0.2 to 0.8 mol%, reaching a maximum in the LBGMO:0.8Yb^{3+},0.1Tm^{3+} sample. A further increase in dopant concentration leads to a decrease in the emission intensity.

In the second series of samples, the Yb^{3+} concentration was fixed at $x = 0.8$, while the Tm^{3+} concentration was varied in the range $y = 0.02$–0.45. The emission spectra under 980 nm excitation are shown in Fig. 4b. Overall, the emission intensity decreases with increasing Tm^{3+} concentration. The highest intensity is observed for the sample LBGMO:0.8Yb^{3+},0.1Tm^{3+}.

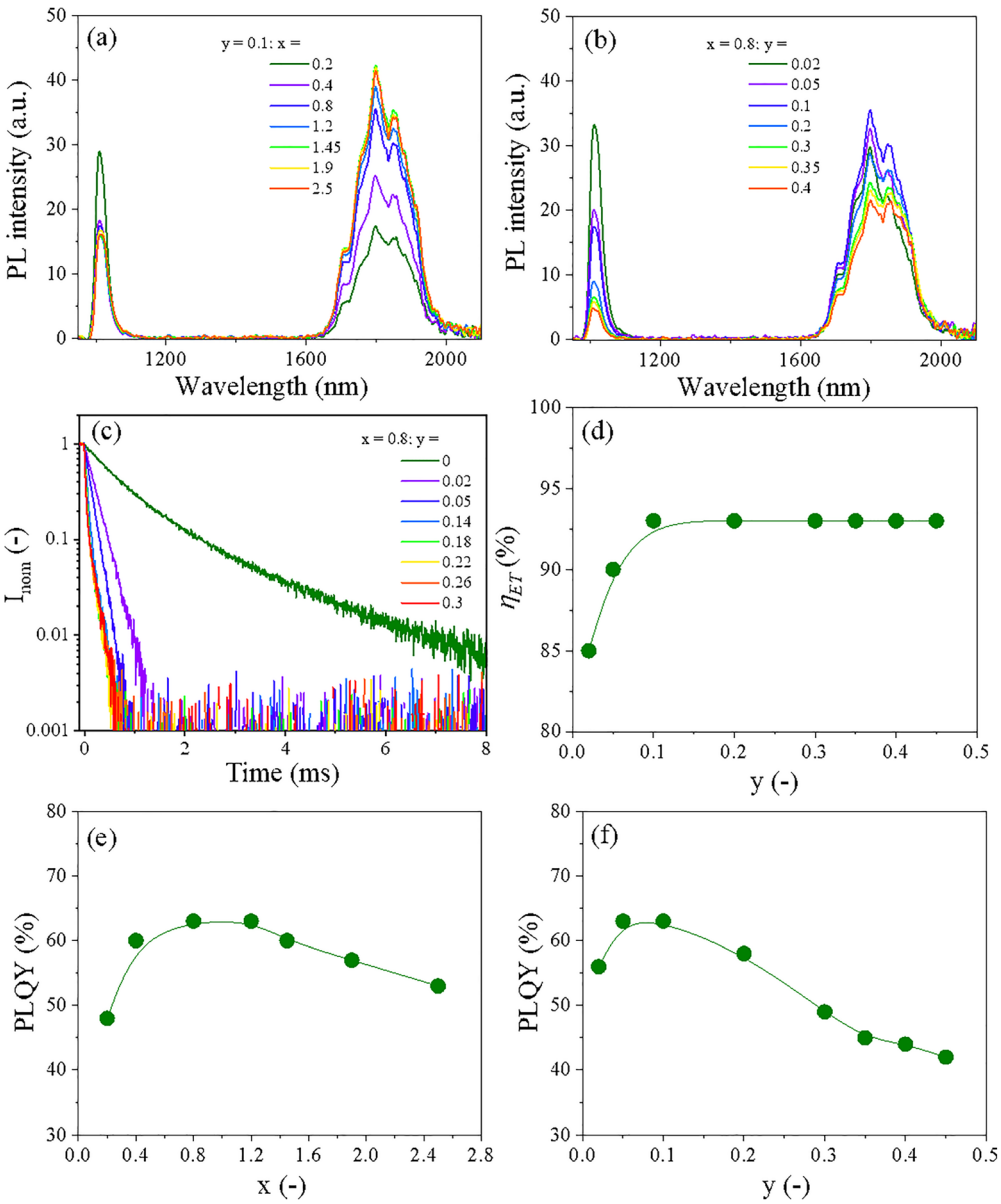

Fig. 4 (a) LDS spectra of the LBGMO:$x$$Yb^{3+}$,0.1$Tm^{3+}$ series of samples under 980 nm excitation; (b) LDS spectra of the LBGMO:0.8Yb^{3+},$y$$Tm^{3+}$ series of samples under 980 nm; (c) LDS decay for the transition $^2F_{5/2} \rightarrow {}^2F_{7/2}$, (at 1027 nm) in LBGMO:0.8Yb^{3+},$y$$Tm^{3+}$ series of samples under 940 nm excitation; (d) efficiency of energy transfer as function of Tm^{3+} concentration in LBGMO:0.8Yb^{3+},$y$$Tm^{3+}$ series of samples; PLQY of the Tm^{3+}: $^3F_4 \rightarrow {}^3H_6$ transition under 980 nm excitation in the (e) LBGMO:$x$$Yb^{3+}$,0.1$Tm^{3+}$ and (f) LBGMO:0.8Yb^{3+},$y$$Tm^{3+}$ series of samples.

A rapid decrease in intensity occurs upon increasing the Tm^{3+} concentration to $y = 0.2$, while further increases result in only minor changes in emission intensity. This behavior is primarily attributed to concentration quenching of Tm^{3+} emission, which is known to become significant for the Tm^{3+}: $^3F_4 \rightarrow {}^3H_6$ transition even at relatively low Tm^{3+} concentrations in glass samples.[53,54]

With the same concentration series, increasing Tm^{3+} content results in a progressive decrease in Yb^{3+} emission intensity, which is attributed to enhanced PAET from Yb^{3+} to Tm^{3+} ions. As the number of Tm^{3+} acceptors increases, the probability of $Yb^{3+} \rightarrow Tm^{3+}$ energy transfer rises, leading to depletion of the Yb^{3+} excited state population and consequently reduced Yb^{3+} emission. Fig. 4c demonstrates LDS decays for of LBGMO:0.8Yb^{3+},yTm^{3+} series of samples. All decays demonstrate complex behaviour which can be described by double exponential fitting. In this case, the average lifetimes were calculated according to the model:

$$I(t) = A_1 \exp\left(-\frac{t}{\tau_1}\right) + A_2 \exp\left(-\frac{t}{\tau_2}\right) \quad (1)$$

and the average lifetime was calculated using the amplitude-weighted method:[55]

$$\langle \tau \rangle = \frac{A_1\tau_1^2 + A_2\tau_2^2}{A_1\tau_1 + A_2\tau_2} \quad (2)$$

To quantitatively evaluate the efficiency of $Yb^{3+} \rightarrow Tm^{3+}$ energy transfer, the transfer efficiency (η_{ET}) was estimated based on the variation of the Yb^{3+} lifetime using the relation:[55]

$$\eta_{ET} = 1 - \frac{\langle \tau_{Yb,Tm} \rangle}{\langle \tau_{Yb} \rangle} \quad (3)$$

The LDS decay measurement of the Yb^{3+}/Tm^{3+} samples were recorded by monitoring the Yb^{3+} emission at 1027 nm ($^2F_{5/2} \rightarrow {}^2F_{7/2}$), shown in Fig. 4c and the results of the fitting are summarized in Table S3. The estimated η_{ET} rises from 83% (at $y = 0.02$) and saturates at 94–95% at concentrations $y > 0.3$ (Fig. 4d). Such a high η_{ET} can be attributed to the strong PAET $Yb^{3+} \rightarrow Tm^{3+}$, as the spectral overlap between Yb^{3+}:$^2F_{5/2}$ and Tm^{3+}:$^3H_5$ is insufficient to support the resonance ET process (Fig. 3a). Additionally, efficient Yb^{3+}–Yb^{3+} energy migration can provide the suitable spatial proximity between Yb^{3+} and Tm^{3+} ions within the LBGMO lattice at a high Yb^{3+} concentration ($x = 0.8$).

The PLQY of both sample series was evaluated under 980 nm excitation (Fig. 4e and f). In the first series, where the Yb^{3+} concentration is varied while Tm^{3+} is kept constant, the PLQY shows an increasing trend with increasing Yb^{3+} content in the range of $x = 0.2$–0.8 (with the highest PLQY of 63% is obtained for the sample LBGMO:0.8Yb^{3+},0.05Tm^{3+}). This is followed by a decrease of PLQY at higher Yb^{3+} concentrations. In the second series, where the Tm^{3+} concentration is systematically varied at a fixed Yb^{3+} content, the PLQY exhibits increase from 56% to 63% at low Tm^{3+} concentration ($y = 0.02$ and 0.05, respectively) and further monotonic decrease with increasing Tm^{3+} concentration. The PLQY drops from approximately 63% to 42% at the highest concentration ($y = 0.45$), reflecting the detrimental effect of concentration quenching and enhanced non-radiative processes at higher Ho^{3+} loadings.

Altogether, the high efficiency of energy transfer and high PLQY of Tm^{3+} SWIR LDS indicate LBGMO host (with cut-off phonon energy of 930 cm^{-1} (ref. 43)) offer good framework for energy transfer from Yb^{3+}:$^2F_{5/2}$ to the Tm^{3+}:$^3H_5$ levels, while multiphonon relaxation and upconversion processes are comparatively weak.

3.3 Optical properties of LBGMO:Yb^{3+}/Ho^{3+}

The optical response of LBGMO co-doped with Yb^{3+} and Ho^{3+} was investigated to elucidate the role of this sensitizer–activator pair in the SWIR range under 980 nm excitation. The DRS (Fig. 5a, green line) exhibits a pronounced absorption band in the 920–1020 nm region, characteristic of the Yb^{3+}: $^2F_{7/2} \rightarrow {}^2F_{5/2}$ transition, confirming that Yb^{3+} ions act as the primary absorbers of the excitation radiation. Superimposed on this feature, weaker absorption bands are observed at ~1150 nm and ~1900 nm, corresponding to the Ho^{3+}: $^5I_8 \rightarrow {}^5I_6$ and Ho^{3+}: $^5I_8 \rightarrow {}^5I_7$ transitions, respectively. It can be assumed that the partial spectral overlap between Yb^{3+} emission and Ho^{3+} absorption enables resonant energy transfer from Yb^{3+} to Ho^{3+}.

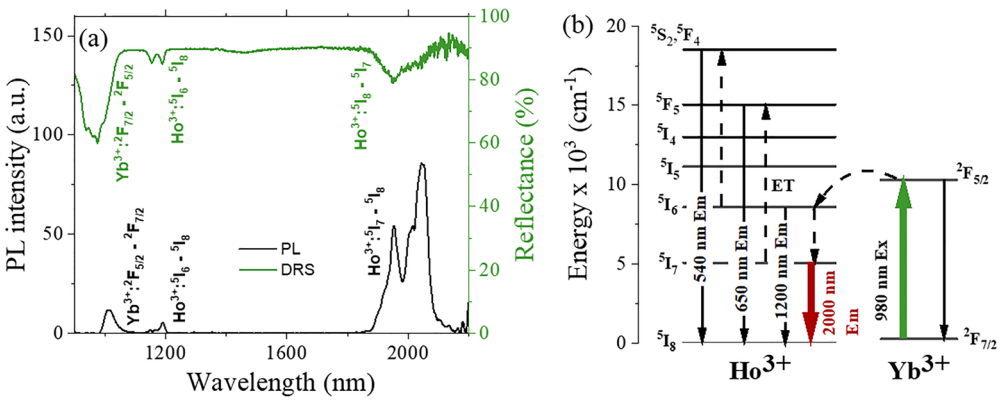

Fig. 5 (a) Representative DRS and LDS spectrum upon 980 nm excitation of the LBGMO:Yb^{3+}/Ho^{3+} phosphor ($x = 2.7$; $y = 0.1$); (b) energy level diagram of the Ho^{3+} and Yb^{3+} ions, solid and dashed lines display radiative and non-radiative processes, respectively.

Under 980 nm excitation, the LDS spectra (Fig. 5a, black line) exhibit three bands assigned to Yb^{3+}: $^2F_{5/2} \rightarrow {}^2F_{7/2}$, Ho^{3+}: $^5I_6 \rightarrow {}^5I_8$ and Ho^{3+}: $^5I_7 \rightarrow {}^5I_8$ transitions. Fig. 5b summarizes the energy level diagram (in addition including possible UC phenomena observed under 980 nm excitation (Fig. S6)) for the Yb^{3+}/Ho^{3+} pair. Notably, Ho^{3+} does not exhibit direct absorption at 980 nm, indicating that efficient $Yb^{3+} \rightarrow Ho^{3+}$ energy transfer is required to achieve the strong SWIR emission. In this process, Yb^{3+} ions absorb 980 nm photons and are excited to the Yb^{3+}:$^2F_{5/2}$ state, followed by non-radiative energy transfer to Ho^{3+}, populating the Ho^{3+}:$^5I_6$ level. Subsequent relaxation occurs *via* two pathways: (i) radiative decay from $^5I_6$ to $^5I_8$, producing emission near ~1200 nm, and (ii) non-radiative relaxation to the $^5I_7$ level, followed by radiative decay to the ground state, yielding emission around ~2000 nm.[56] The observed broad emission band of Ho^{3+} centered near 2000 nm, with FWHM of ~150 nm, indicates substantial crystal-field splitting of the Ho^{3+} 4f levels, which can be attributed to the low site symmetry of the LBGMO host.

To further investigate the LDS in the LBGMO:Yb^{3+},Ho^{3+} phosphors, two series of samples were examined. The first one had the Ho^{3+} doping fixed at y = 0.1 and Yb^{3+} doping varied in the x = 0.2 to 2.7 range. The emission spectra are presented in Fig. 6a. All spectra exhibit similar emission

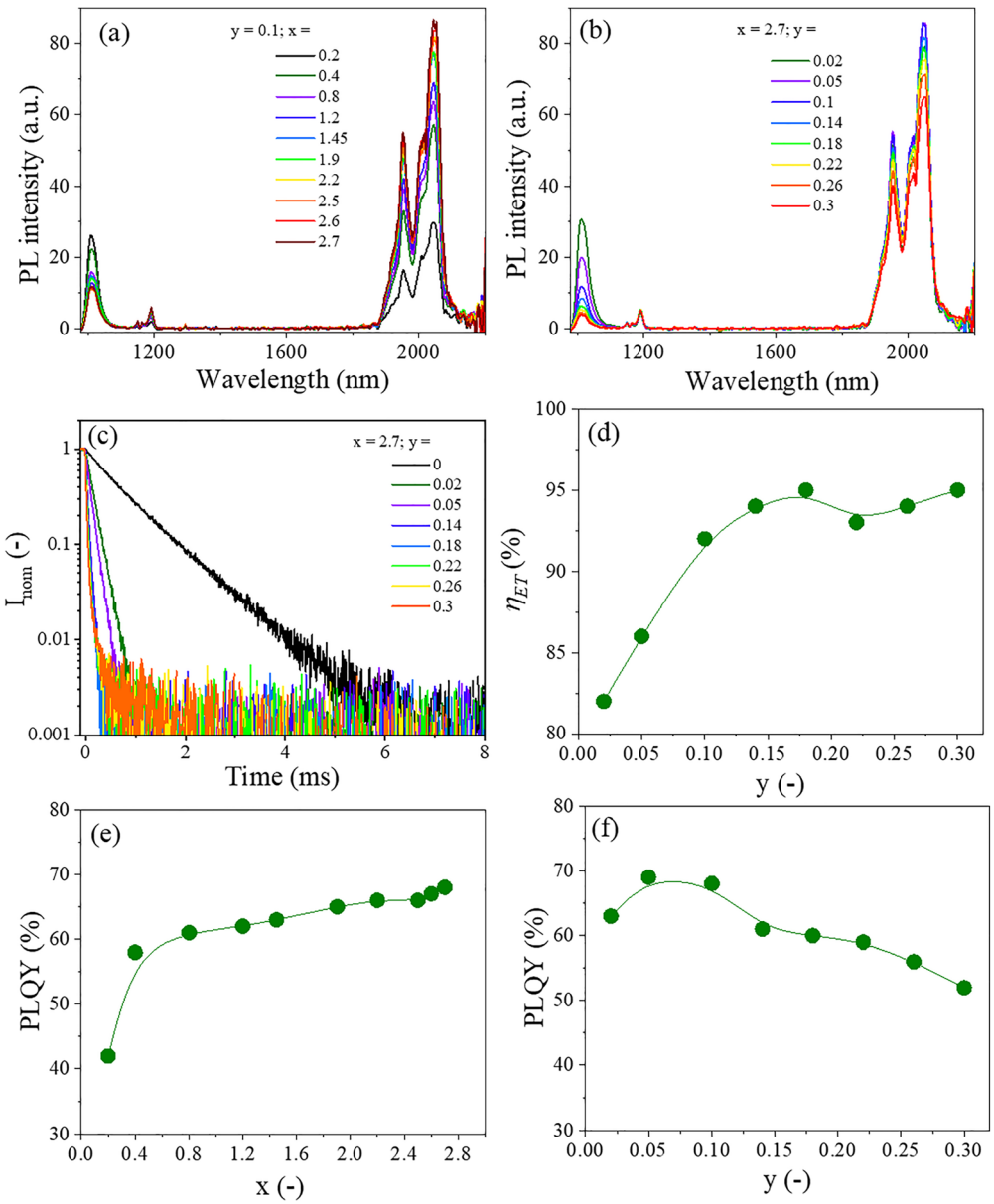

Fig. 6 (a) LDS spectra of the LBGMO:$x$$Yb^{3+}$,0.1$Ho^{3+}$ series of samples under 980 nm excitation; (b) LDS spectra of the LBGMO:2.7Yb^{3+},$y$$Ho^{3+}$ series of samples under 980 nm; (c) LDS decay (Yb^{3+}: $^2F_{5/2} \rightarrow {}^2F_{7/2}$ at 1027 nm) of LBGMO:2.7Yb^{3+},$y$$Ho^{3+}$ series of samples under 940 nm excitation; (d) efficiency of energy transfer as function of Ho^{3+} concentration in LBGMO:2.7Yb^{3+},$y$$Ho^{3+}$ series of samples; PLQY of the Ho^{3+}: $^5I_7 \rightarrow {}^5I_8$ transition under 980 nm excitation in the (e) LBGMO:$x$$Yb^{3+}$,0.1$Ho^{3+}$ and (f) LBGMO:2.7Yb^{3+},$y$$Ho^{3+}$ series of samples.

features. The emission intensity of the Ho^{3+}: $^5I_7 \rightarrow {}^5I_8$ transition increases gradually with increasing Yb^{3+} concentration, reaching a maximum at the highest Yb^{3+} doping level (x = 2.7). The second series of samples had the Yb^{3+} doping fixed at x = 2.7 and the Ho^{3+} doping varied over the y = 0.02 to 0.3 range. The emission spectra under 980 nm excitation are presented in Fig. 6b, indicating that the maximum intensity of the Ho^{3+}: $^5I_7 \rightarrow {}^5I_8$ emission band is achieved at a Ho^{3+} co-doping concentration of y = 0.05. Further increasing the Ho^{3+} concentration leads to a steep decrease in the LDS intensity.

To quantitatively evaluate the efficiency of $Yb^{3+} \rightarrow Ho^{3+}$ energy transfer, the transfer efficiency (η_{ET}) was estimated based on eqn (3). The LDS decay curves of the Yb^{3+}/Ho^{3+} samples were recorded by monitoring the Yb^{3+} emission at 1027 nm ($^2F_{5/2} \rightarrow {}^2F_{7/2}$), shown in Fig. 6c and results of the fitting are summarized in Table S4. The estimated η_{ET} rises from 83% (at y = 0.02) and saturates at 95–96% at concentrations $y > 0.18$ (Fig. 6d). Such a high η_{ET} can be again attributed to the strong phonon-assisted energy transfer $Yb^{3+} \rightarrow Ho^{3+}$ (although the spectral overlap between Yb^{3+}:$^2F_{5/2}$ and Ho^{3+}:$^5I_6$ is minimal, as can be observed in Fig. 5a) and efficient Yb^{3+}–Yb^{3+} energy migration so that the suitable spatial proximity between Yb^{3+} and Tm^{3+} ions in the LBGMO lattice at high Yb^{3+} concentration (x = 2.7). To further support the proposed $Yb^{3+} \rightarrow Tm^{3+}$ and $Yb^{3+} \rightarrow Ho^{3+}$ energy-transfer, additional PLE measurements were performed. The SWIR emission was monitored in the ranges 1700–1900 nm for Tm^{3+}-*co*-doped samples and 1900–2100 nm for Ho^{3+}-*co*-doped samples, while the excitation wavelength was scanned across the Yb^{3+} absorption band (900–990 nm). The resulting PLE spectra, included as Fig. S7, closely reproduce the Yb^{3+} absorption, providing additional evidence that the observed SWIR emission originates from Yb^{3+}-sensitized excitation followed by energy transfer to Tm^{3+} or Ho^{3+} ions.

The next step is to examine the PLQY of both compositional series under 980 nm excitation. In the first series, where the Yb^{3+} concentration is varied while Ho^{3+} is kept constant, the PLQY shows an overall increasing trend with increasing Yb^{3+} content. A pronounced enhancement is observed at low Yb^{3+} concentrations, where the PLQY rises rapidly from approximately 42% to 58% as x increases from 0.2 to 0.4. With further Yb^{3+} incorporation, the increase becomes more gradual, reaching a maximum of 68% at x = 2.7 (Fig. 6e), indicating a progressive improvement in sensitization efficiency, followed by a tendency toward saturation.

In the second series, where the Ho^{3+} concentration is systematically varied at a fixed Yb^{3+} content, the PLQY exhibits an increase from 63% to 69% at low Ho^{3+} concentration (y = 0.02 and 0.05, respectively) and clear further monotonic decrease with increasing Ho^{3+} concentration (Fig. 6f). The PLQY drops from approximately 69% at the lowest Ho^{3+} level to 52% at the highest concentration (y = 0.3), reflecting the detrimental effect of concentration quenching and enhanced non-radiative processes at higher Ho^{3+} loadings. The highest PLQY is achieved at low Ho^{3+} concentration (y = 0.05) in combination with x = 2.7 of Yb^{3+}, where efficient $Yb^{3+} \rightarrow Ho^{3+}$ energy transfer and minimized cross-relaxation collectively result in an impressive maximum PLQY of 69%.

These spectral characteristics indicate that energy transfer from Yb^{3+}:$^2F_{5/2}$ to the Ho^{3+} excited states (particularly $^5I_6$) is highly efficient. These results also suggest that the combination of high emission intensity and broad spectral bandwidth highlights the potential of Yb^{3+}/Ho^{3+} co-doped LBGMO as an efficient solid-state SWIR emitter for pc-LED applications operating within the SWIR range.

3.4 Performance of LBGMO:Yb^{3+}/Tm^{3+} and LBGMO:Yb^{3+}/Ho^{3+} fabricated pc-LED device

The performance of the phosphor conversion layers was evaluated quantitatively in terms of WPE, defined as the ratio of the emitted optical power (measured in Watts using an integrating sphere) to the electrical power supplied to the LED device. As these materials are intended for use in spectral conversion for SWIR pc-LEDs, their performance was assessed under device-relevant operating conditions to ensure practical relevance. To mimic real device architectures, compositions with the highest PLQYs – LBGMO:0.8Yb^{3+},0.1Tm^{3+} and LBGMO:2.7Yb^{3+},0.1Ho^{3+} – were dispersed homogeneously in a silicone resin matrix and then deposited onto 940 nm LED chips to form integrated spectral conversion layers (Fig. S8).

Prior to the WPE evaluation, the temperature-dependent LDS properties of the LBGMO:0.8Yb^{3+},0.1Tm^{3+} and LBGMO:2.7Yb^{3+},0.1Ho^{3+} phosphors were investigated over the temperature range of 293–478 K (20–200 °C). As shown in Fig. 7a,b and 8a,b, both phosphors exhibit good thermal stability. At 478 K, the integrated LDS intensity remained at 89% and 90% of its initial value at 293 K for the Tm^{3+}- and Ho^{3+}-doped phosphors, respectively.

The resulting NIR emission characteristics were investigated by measuring the emitted SWIR optical power as a function of the applied driving current. In particular, emissions centered at approximately 1800 nm (corresponding to Tm^{3+} transitions, see Fig. 7c) and at approximately 2050 nm (arising from Ho^{3+} emission, see Fig. 8c) were monitored. The corresponding WPE values were extracted from these measurements and plotted as a function of current density (Fig. 7d and 8d), enabling a direct assessment of device-level performance and efficiency under realistic operating conditions.

For the device incorporating the LBGMO:0.80Yb^{3+},0.1Tm^{3+} conversion layer (LED940@Tm), a maximum WPE of 1.6% was achieved at a driving current of 50 mA. Upon increasing the current to 300 mA, the WPE gradually decreased to approximately 1.1%, indicating a current-dependent efficiency roll-off. For comparison, the uncoated 940 nm LED exhibits a WPE of ~40% (Fig. S9) under similar operating conditions, indicating that the overall device efficiency is predominantly limited by optical losses. The reduction in WPE after phosphor integration can be attributed to non-radiative losses associated with PLQY < 100%. Furthermore, thermal effects at higher drive currents contribute to the observed efficiency roll-off (see insert in Fig. 7d), which demonstrates an increase of chip

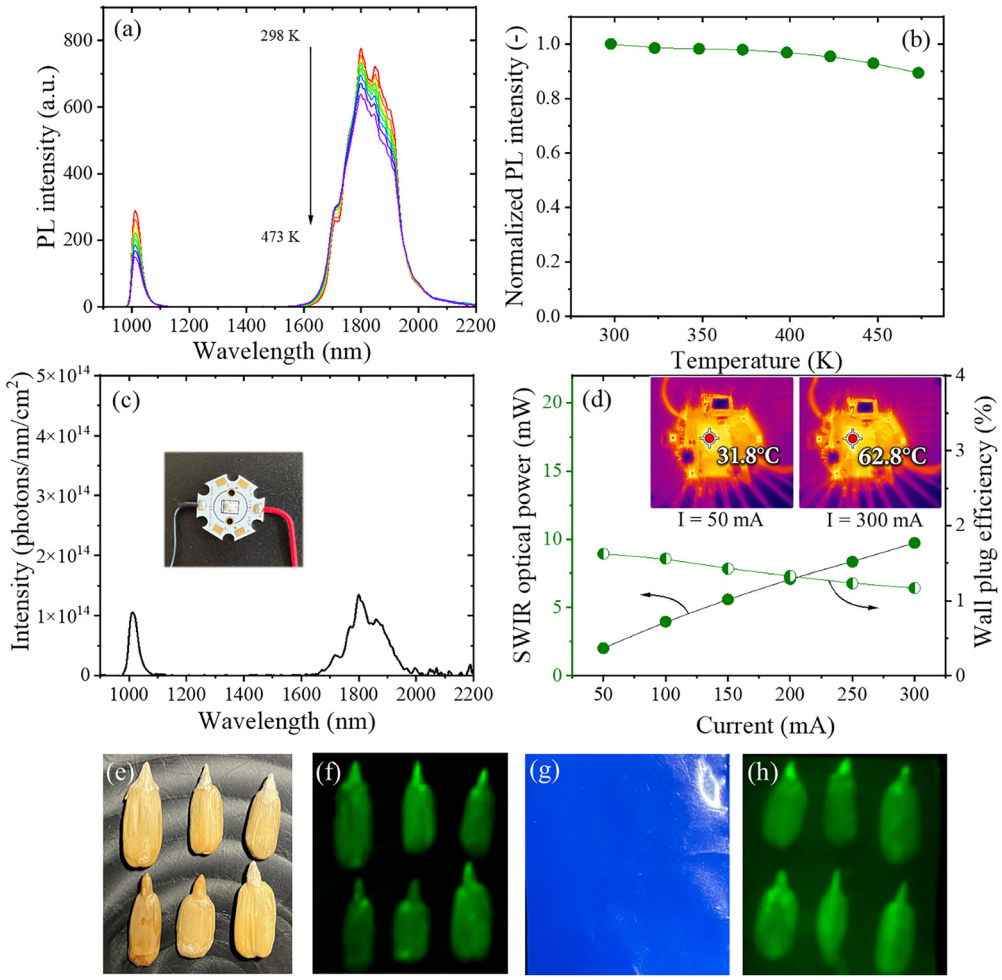

Fig. 7 (a) Temperature-dependent LDS spectra of the LBGMO:0.8Yb^{3+},0.1Tm^{3+} phosphor under 940 nm excitation; (b) normalized integrated LDS intensity of the LBGMO:0.8Yb^{3+},0.1Tm^{3+} phosphor in the 1600–2200 nm spectral range as a function of temperature; (c) emission spectrum of 940 nm LED chip coated with with LBGMO:0.8Yb^{3+},0.1Tm^{3+} phosphor (LED940@Tm) (the insert demonstrates the LED940@Tm chip); (d) SWIR power output and WPE of LED940@Tm chip (inserts demonstrate chip temperature at current of 50 and 300 mA); (e) photograph of sunflower seeds illuminated by a halogen lamp and captured using an iPhone 16 camera; (f) false-color SWIR image of the same seeds acquired using a hyperspectral SWIR camera under illumination from the LED940@Tm chip; (g) photograph of sunflower seeds covered with a polyethylene film opaque to visible light, captured using an iPhone 16 camera under halogen lamp illumination; (h) false-color SWIR image of the same seeds covered with the polyethylene film and acquired using a hyperspectral SWIR camera under illumination from the LED940@Tm chip.

temperature from 31.8 °C (at current of 50 mA) up to 62.8 °C (at current of 300 mW).

Under identical fabrication and measurement conditions, the device based on the LBGMO:2.7Yb^{3+},0.05Ho^{3+} layer (LED940@Ho) exhibited a markedly higher WPE of 3.6% at 50 mA. With increasing drive current up to 300 mA, the WPE decreased to approximately 2.6%, while remaining substantially higher than that of the Tm^{3+}-based system across the entire current range. The thermal effects at higher drive currents again contribute to the observed efficiency roll-off (see insert in Fig. 8d), which demonstrates an increase of chip temperature from 35.2 °C (at current of 50 mA) up to 113.2 °C (at current of 300 mW).

The used 940 nm AlGaAs/GaAs surface-emitting chip represents one of the most cost-efficient LED platforms (along with the 850 nm AlGaAs/GaAs chip).[57] However, it is also worthwhile to explore the less common 980 nm LED chip (Fig. S10), which is typically based on an InGaAs/AlGaAs or InGaAs/GaAs architecture and emits in the spectral range corresponding to the maximum absorption of Yb^{3+} ions. The performance of the light-conversion layer based on the 980 nm chip is presented in Fig. S11. Overall, these devices demonstrate a slightly higher WPE at the same driving current (for instance, 1.7% and 5.1% at 50 mA for LED980@Tm and LED980@Ho, respectively). This improvement is likely attributed to the stronger absorption of 980 nm radiation compared with 940 nm radiation.

Furthermore, the LED940@Tm and LED940@Ho devices were used in SWIR imaging applications. Fig. 7e and f demonstrate imaging of seeds under visible light illumination using a halogen lamp and a 940 nm LED source (LED940@Tm), respectively. The two images exhibit comparable contrast and spatial features. In contrast, Fig. 7g and h highlight the

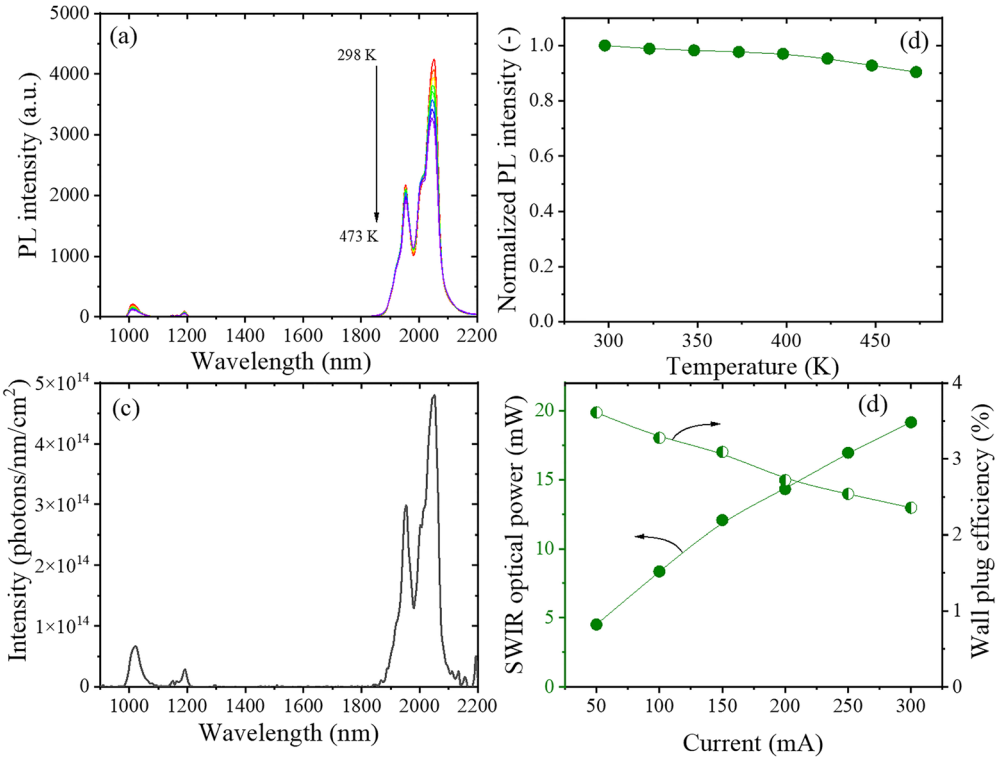

Fig. 8 (a) Temperature-dependent LDS spectra of the LBGMO:2.7Yb^{3+},0.1Ho^{3+} phosphor under 940 nm excitation; (b) normalized integrated LDS intensity of the LBGMO:2.7Yb^{3+},0.1Ho^{3+} phosphor in the 1600–2200 nm spectral range as a function of temperature; (c) emission spectrum of 940 nm LED chip coated with with LBGMO:2.7Yb^{3+},0.1Ho^{3+} phosphor (LED940@Ho) (the insert demonstrates the LED940@Ho chip); (d) SWIR power output and WPE of LED940@Ho chip (inserts demonstrate chip temperature at current of 50 and 300 mA).

capability of SWIR-sensitive imaging to penetrate a polymer film that is completely opaque in the visible spectral range. In Fig. 7g, the halogen-illuminated scene captured with a standard visible-range camera shows only a strong specular reflection from the polymer surface, with no information from the seeds beneath the film. However, Fig. 7h, acquired using SWIR illumination from the LED940@Tm chip and detected by a hyperspectral SWIR camera, clearly reveals the spatial positions and shapes of the seeds through the polymer barrier.

The emission characteristics of the LED940@Ho illumination source demonstrate overlap with a strong absorption band of water centered around ~1900 nm, indicating that even small differences in moisture content produce measurable changes in reflected intensity. As a result, the optical system becomes inherently sensitive to the presence of water inside biological samples such as seeds. In Fig. 9a and b, the physical appearance of seeds and their corresponding SWIR reflectance images are shown, respectively. In the visible-range photograph (Fig. 9a), wet and dry seeds appear largely similar, making reliable visual discrimination difficult or impossible. However, once the same seeds are illuminated under the LED940@Ho-based SWIR imaging configuration (Fig. 9b), clear contrast emerges between individual seeds. This contrast is not based on surface color or morphology, but on differences in internal water absorption affecting the reflected SWIR signal. Wet seeds generally appear darker or exhibit altered intensity patterns compared to dry seeds due to stronger absorption of radiation in water-sensitive wavelengths. This behavior is quantitatively confirmed in the spectral profiles presented in Fig. 9c. The hyperspectral SWIR camera records reflectance spectra from each seed, revealing divergence between wet and dry samples. Wet seeds show reduced reflectance (or stronger absorption features) in the 1900 nm region. The separation between the two spectral curves provides a robust optical signature of moisture content. Based on this spectral separation, a simplified classification rule can be defined, as illustrated in Fig. 9d. Instead of performing full spectral analysis, a decision-making criterion can be reduced to a threshold-based or ratio-based metric derived from selected wavelength bands, particularly those sensitive to water absorption. This enables rapid differentiation between wet and dry seeds using hyperspectral data.

Importantly, Fig. 9e–h further demonstrate the robustness of this method, showing that the same wet-*versus*-dry discrimination can be successfully performed even when the seeds are covered by a non-transparent film in the visible spectral range. Although the coating obscures all visual information in standard imaging (Fig. 9e), SWIR-based measurement remains effective because SWIR radiation can partially penetrate through the polymer film. The corresponding spectral signatures (Fig. 9g) still demonstrates the difference between wet and dry seeds, and the classification map (Fig. 9h) indicates that accurate segmentation is possible despite optical occlusion in the visible spectrum.

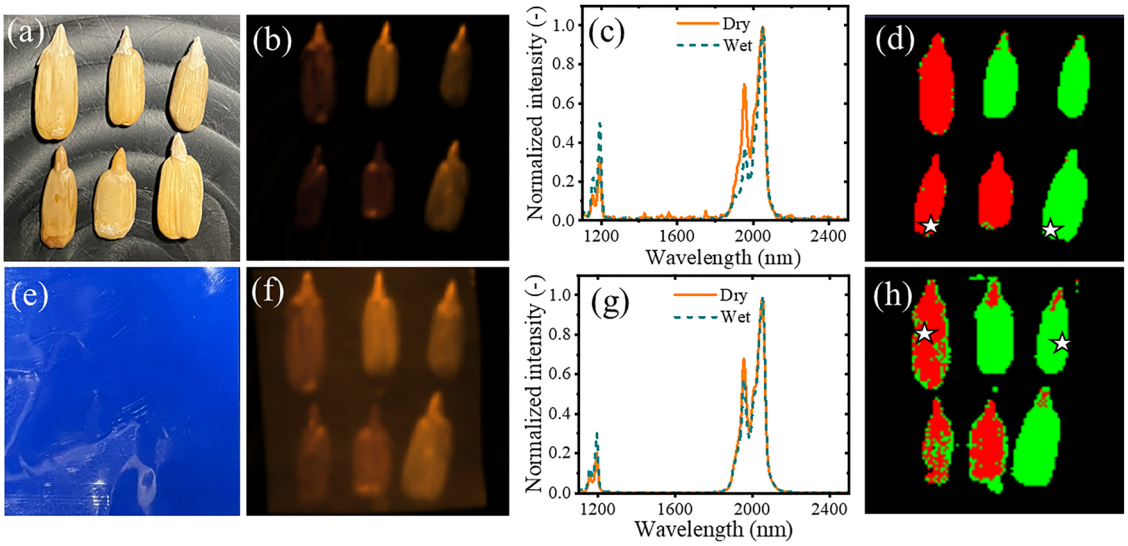

Fig. 9 (a) image of seeds illuminated with a halogen lamp, captured with an iPhone 16 camera; (b) false-color SWIR image of the same seeds illuminated with the coated LED chip (LED940@Ho), captured with the hyperspectral SWIR camera; (c) spectra of the wet and dry seeds obtained with the hyperspectral SWIR camera; (d) false-colour interpretation for decision-making to differentiate between wet and dry seeds. White stars demonstrate pixels corresponding to spectra in (c); (e) image of the seeds covered with a polyethylene film opaque to visible light, captured with an iPhone 16 camera under halogen lamp illumination; (f) false-color SWIR image of the same seeds covered with a polyethylene film opaque to visible light, captured with a hyperspectral SWIR camera under illumination from the LED940@Ho chip; (g) spectra of the wet and dry seeds with a polyethylene film opaque to visible light, obtained with the hyperspectral SWIR camera; (h) false-colour interpretation for decision-making to differentiate between wet and dry seeds covered with a polyethylene film opaque to visible light. White stars demonstrate pixels corresponding to spectra in (g).

4. Conclusions

The obtained results demonstrate that the well-defined spectral positions, broad emission bands, and high PLQYs of the LBGMO host doped with Yb^{3+}/Tm^{3+} and Yb^{3+}/Ho^{3+} ion pairs make these phosphors suitable for use as spectral conversion layers in SWIR-emitting pc-LEDs. Under 940 nm excitation, Tm^{3+} ions are efficiently populated at the $^3F_4$ level, resulting in broadband emission centered at approximately 1800 nm. In the Yb^{3+}/Ho^{3+} system, efficient population of the $^5I_7$ state leads to dominant emission near 2050 nm. The strong SWIR emission is accompanied by high PLQY values of 63% for the Tm^{3+}-doped sample and 69% for the Ho^{3+}-doped sample. These results are associated with efficient energy transfer from Yb^{3+} to Tm^{3+} (95%) and from Yb^{3+} to Ho^{3+} (96%), together with the moderate cut-off phonon energy of 930 cm^{-1}, which supports efficient population of the lower-energy SWIR-emitting states.

These findings identify LBGMO as a structurally stable and electronically suitable host lattice for efficient long-wavelength NIR emission in the 1600–2200 nm spectral range under 940 nm excitation. In addition, pc-LED devices incorporating Yb^{3+}/Tm^{3+} and Yb^{3+}/Ho^{3+} conversion layers achieve maximum wall-plug efficiencies of 1.6% and 3.6%, respectively, demonstrating their practical potential. As an example, the LED device containing the Yb^{3+}/Tm^{3+} conversion layer was successfully used for SWIR imaging through a film opaque in the visible spectral range. The emission of this device also overlaps with a strong water absorption band, indicating potential applicability for water detection.

Overall, the results demonstrate that LBGMO-based Yb^{3+}-sensitized phosphors represent a promising material platform for efficient SWIR pc-LEDs, combining high LDS performance with device-level functionality.

Conflicts of interest

There are no conflicts to declare.

Data availability

The data that support the findings of this study are available from the corresponding authors upon reasonable request.

Supplementary information includes comparison of representative SWIR light sources, Rietveld refinement and XRD analyses, photoluminescence characterization, fabrication of spectral conversion layers, and optical and thermal characterization of SWIR phosphor-converted LEDs. See DOI: https://doi.org/10.1039/d6mh00984k.

Acknowledgements

The Helmholtz Association is gratefully acknowledged: (i) a Recruitment Initiative Fellowship for B. S. R.; and (ii) Research Field Energy – Program Materials and Technologies for the Energy Transition – Topic 1 Photovoltaics (38.01.02). The authors acknowledge Dr. Guojun Gao (Polysecure GmbH) for performing particle size analysis.

References

1 L. Guanter, H. Kaufmann, K. Segl, S. Foerster, C. Rogass, S. Chabrillat, T. Kuester, A. Hollstein, G. Rossner, C. Chlebek, C. Straif, S. Fischer, S. Schrader, T. Storch, U. Heiden, A. Mueller, M. Bachmann, H. Mühle, R. Müller, M. Habermeyer, A. Ohndorf, J. Hill, H. Buddenbaum, P. Hostert, S. Van der Linden, P. J. Leitão, A. Rabe, R. Doerffer, H. Krasemann, H. Xi, W. Mauser, T. Hank, M. Locherer, M. Rast, K. Staenz and B. Sang, The EnMAP Spaceborne Imaging Spectroscopy Mission for Earth Observation, *Remote Sens.*, 2015, 8830–8857.

2 H. Song, S. Yeo, Y. Jin, I. Park, H. Ju, Y. Nalcakan and S. Kim, Short-Wave Infrared (SWIR) Imaging for Robust Material Classification: Overcoming Limitations of Visible Spectrum Data, *Appl. Sci.*, 2024, 11049.

3 S. International Organization for, Optics and photonics—Spectral bands, ISO 20473:2007 (2007).

4 Y. Chen, L. Xue, Q. Zhu, Y. Feng and M. Wu, Recent Advances in Second Near-Infrared Region (NIR-II) Fluorophores and Biomedical Applications, *Front. Chem.*, 2021, **9**, 750404.

5 L. Shi, L. A. Sordillo, A. Rodríguez-Contreras and R. Alfano, Transmission in near-infrared optical windows for deep brain imaging, *J. Biophotonics*, 2016, **9**(1–2), 38–43.

6 D. Roblyer, A. Pilvar, T. Pham, S. Spink, C. K. Hayakawa, V. Venugopalan and M. C. Pierce, Review of shortwave infrared imaging and spectroscopy in tissue [Invited], *Biomed. Opt. Express*, 2025, **16**(12), 5028–5062.

7 Y. Chang, H. Chen, X. Xie, Y. Wan, Q. Li, F. Wu, R. Yang, W. Wang and X. Kong, Bright Tm^{3+}-based downshifting luminescence nanoprobe operating around 1800 nm for NIR-IIb and c bioimaging, *Nat. Commun.*, 2023, **14**(1), 1079.

8 Z. Xing, Q. Hu, W. Wang, N. Kong, R. Gao, X. Shen, S. Xu, L. Meng, J.-R. Liu and X. Zhu, An NIR-IIb emissive transmembrane voltage nano-indicator for the optical monitoring of electrophysiological activities in vivo, *Mater. Horiz.*, 2024, **11**(10), 2457–2468.

9 X. Wang, J. Du, D. Hreniak, W. Stręk, K. Jiang and H. Lin, Construction of an Fe–Ni energy bridge for NIR-II luminescence enhancement and anti-thermal quenching via microwave-induced defect engineering, *Mater. Horiz.*, 2025, **12**(14), 5277–5286.

10 G. Benjamin and L. Peter, Review on short-wavelength infrared laser gated-viewing at Fraunhofer IOSB, *Opt. Eng.*, 2016, **56**(3), 031203.

11 T. Siegel and S.-P. Chen, Investigations of Free Space Optical Communications Under Real-World Atmospheric Conditions, *Wirel. Pers. Commun.*, 2021, **116**(1), 475–490.

12 N. Lopac, I. Jurdana, A. Brnelić and T. Krljan, Application of Laser Systems for Detection and Ranging in the Modern Road Transportation and Maritime Sector, *Sensors*, 2022, 5946.

13 Y. Zheng, J. Bai, J. Xu, X. Li and Y. Zhang, A discrimination model in waste plastics sorting using NIR hyperspectral imaging system, *Waste Manage.*, 2018, **72**, 87–98.

14 S. L. Kühn, S. C. Iden, F. Kästner and M. Sut-Lohmann, Tracking soil moisture dynamics with Vis-NIR spectroscopy during laboratory bare-soil evaporation, *Geoderma*, 2025, **459**, 117368.

15 G. Bonifazi, R. Gasbarrone, D. Gattabria, E. Lendaro, L. Mosca, R. Mattioli and S. Serranti, Early Study on Visible (Vis) and Short-Wave Infrared (SWIR) Spectroscopy for Assessing Water Content in Olive Fruits: Towards Sustainable Land and Agricultural Practices, *Land*, 2024, 2231.

16 W. Chen, Y. Wang, G. Liu, C. Li and Z. Xia, Phosphor-in-Ceramic-Converted Laser-Driven Near-Infrared Light Sources for Multiple Intelligent Spectroscopy Applications, *Adv. Mater.*, 2024, **36**(52), 2413857.

17 Y. Liu, K. Liu, J. Song, Y. Chang, B. Kang, J. Yin and G. Du, 1.3 μm integrated superluminescent light source, *Opt. Mater.*, 2000, **14**(3), 235–238.

18 Ushio, Inc. https://www.ushio.co.jp/en/products/product_file/file/SLC1750D-1100-G03-X.pdf, (accessed 26.06.2026).

19 Y. Arslan, F. Oguz and C. Besikci, Extended wavelength SWIR InGaAs focal plane array: Characteristics and limitations, *Infrared Phys. Technol.*, 2015, **70**, 134–137.

20 S. Park, P. D. Nguyen, Y. Kim, J. Jeon, M. R. McCartney, D. J. Smith, M. Kim, D. Kim, B. S. Chun and S. J. Lee, Metamorphic InGaAs/InAsPSb Quantum Well Light Emitting Diodes for Operation in the Short-Wave Infrared Region, *Adv. Funct. Mater.*, 2024, **34**(45), 2406355.

21 M. Buffolo, A. Magri, C. De Santi, G. Meneghesso, E. Zanoni and M. Meneghini, Gradual Degradation of InGaAs LEDs: Impact on Non-Radiative Lifetime and Extraction of Defect Characteristics, *Materials*, 2021, 1114.

22 Y. Guo, S. Wei, F. Liu, A. Li, Z. Lu, Z. Zhao, B. Wang and L. Chen, Near-Infrared Phosphor Zn_2InGaO_5:Cr^{3+} with a Wide Bandgap Applicable for Light Sources at Low Temperature, *ACS Appl. Opt. Mater.*, 2025, **3**(4), 828–838.

23 M. Sójka, J. Zhong and J. Brgoch, Developing Broadband Cr^{3+} -Substituted Phosphor-Converted Near-Infrared Light Sources, *ACS Appl. Opt. Mater.*, 2023, **1**(6), 1138–1149.

24 Y. Wang, C. Ran, Y. Wang, F. Wu, Q. Zhang, Y. Teng, H. Dong, X. Zhang and Z. Mu, Design of $Mg_6Ga_8GeO_{20}$:Cr^{3+}, Ni^{2+} near infrared phosphors and application research of NIR pc-LED based on efficient Cr^{3+} to Ni^{2+} energy transfer, *J. Photochem. Photobiol., A*, 2026, **478**, 117167.

25 Spectrum of tungsten-halogen lamp. https://www.thorlabs.com/tungsten-halogen-light-source?tabName=Overview, (accessed 26.06.2026).

26 Spectrum of xenon arc lamp. https://www.thorlabs.com/xenon-arc-light-sources?pn=SLS402&tabName=Overview, (accessed 26.06.2026).

27 Xe-Arc lamp SWIR. https://mmrc.caltech.edu/Stark/Xe%20-lamp%20spectra.pdf?utm_source=chatgpt.com. (accessed 26.06.2026).

28 S. Miao, Y. Liang, R. Shi, W. Wang, Y. Li and X.-J. Wang, Broadband Short-Wave Infrared-Emitting $MgGa_2O_4$:Cr^{3+}, Ni^{2+} Phosphor with Near-Unity Internal Quantum Efficiency and High Thermal Stability for Light-Emitting Diode Applications, *ACS Appl. Mater. Interfaces*, 2023, **15**(27), 32580–32588.

29 Superlum. https://www.superlumdiodes.com/pdf/S1585_MP_rev01.pdf, (accessed 26.06.3026).

30 InGaAs LED. https://tech-led.com/wp-content/uploads/2024/05/SMBB1900D-1100.pdf, (accessed 26.06.2026).
31 GaSb laser. https://www.coherent.com/content/dam/coherent/site/en/resources/datasheet/components-and-accessories/mir-laser-1850-2300nm-ds.pdf, (accessed 26.06.2026).
32 Tm-doped fiber lasers. https://www.thorlabs.com/thulium-doped-fiber-lasers?tabName=Graphs, (accessed 26.06.2026).
33 F. Arteaga Cardona, N. Jain, R. Popescu, D. Busko, E. Madirov, B. A. Arús, D. Gerthsen, A. De Backer, S. Bals, O. T. Bruns, A. Chmyrov, S. Van Aert, B. S. Richards and D. Hudry, Preventing cation intermixing enables 50% quantum yield in sub-15 nm short-wave infrared-emitting rare-earth based core-shell nanocrystals, *Nat. Commun.*, 2023, **14**(1), 4462.
34 H.-H. Li, Y.-K. Wang and L.-S. Liao, Near-Infrared Luminescent Materials Incorporating Rare Earth/Transition Metal Ions: From Materials to Applications, *Adv. Mater.*, 2024, **36**(30), 2403076.
35 N. Bednarska-Adam, M. Kuwik, T. Goryczka, V. Ivanov, J. Dresner, W. A. Pisarski and J. Pisarska, Near-infrared luminescence from Li_2ZnGeO_4:Ln^{3+} (Ln = Er, Tm, Ho), *RSC Adv.*, 2025, **15**(11), 8784–8794.
36 K. Rajagopalan, G. Gao, L. J. B. Erasmus, D. Busko, B. S. Richards and A. Turshatov, Boosting the brightness of short-wave infrared emission in YPO_4:Yb^{3+}/Er^{3+} phosphors: optimal photoluminescence quantum yield versus particle size, *Mater. Adv.*, 2026, **7**(3), 1852–1865.
37 K. Suresh and C. K. Jayasankar, Conversion of blue-green photon into NIR photons in Ho^{3+}/Yb^{3+} co-doped zinc tellurite glasses, *J. Alloys Compd.*, 2019, **788**, 1048–1055.
38 J. Markiewicz, M. Kochanowicz, T. Ragiń, K. Sadowska, J. Żmojda, P. Miluski, J. Dorosz, M. Kuwik, W. A. Pisarski, J. Pisarska, M. Leśniak and D. Dorosz, Broadband 1.5-2.1 μm emission in gallo-germanate dual-core optical fiber co-doped with Er^{3+} and Yb^{3+}/Tm^{3+}/Ho^{3+}, *Opt. Express*, 2023, **31**(18), 28850–28858.
39 R. Fartas, M. Diaf, I. R. Martin, F. Paz-Buclatin and J. P. Jouart, Near infrared and upconversion luminescence of Tm^{3+}–Yb^{3+} codoped CdF_2 single crystals, *J. Lumin.*, 2020, **228**, 117594.
40 K. A. Pierpoint, M. E. Doroshenko, O. K. Alimov, A. G. Papashvili, V. A. Konyushkin, A. N. Nakladov and A. V. Nekhoroshikh, Spectroscopic properties of Ho^{3+} optical centers in CaF_2 crystals at the two-micron laser transition, *J. Lumin.*, 2020, **228**, 117584.
41 X. Pan, P. Yu, Z. Wang, F. Yu and X. Xu, Growth and spectroscopic properties of Tm^{3+} doped YPO_4 crystal, *CrystEngComm*, 2023, **25**(14), 2104–2109.
42 Y. Zhang, H. Zhu, X. Yang, H. Wang, Q. Wang, C. Sun, H. Tian and H. Liu, Visible to infrared wide wavelength range luminescence of Sr_2LaNbO_6: Yb^{3+}/Nd^{3+}/Ho^{3+} phosphor under 808/980 nm excitation and temperature sensing application, *Spectrochim. Acta, Part A*, 2025, **326**, 125199.
43 K. Rajagopalan, E. Madirov, D. Busko, I. A. Howard, B. S. Richards, H. C. Swart and A. Turshatov, High Quantum Yield Shortwave Infrared Luminescent Tracers for Improved Sorting of Plastic Waste, *ACS Appl. Mater. Interfaces*, 2023, **15**(37), 43985–43993.
44 E. Madirov, D. Busko, F. A. Cardona, D. Hudry, S. V. Kuznetsov, V. A. Konyushkin, A. N. Nakladov, A. A. Alexandrov, I. A. Howard, B. S. Richards and A. Turshatov, Comparison of Quantum Yield of Upconversion Nanocrystals Determined by Absolute and Relative Methods, *Adv. Photonics Res.*, 2023, **4**(2), 2200187.
45 S. Leyre, E. Coutino-Gonzalez, J. J. Joos, J. Ryckaert, Y. Meuret, D. Poelman, P. F. Smet, G. Durinck, J. Hofkens, G. Deconinck and P. Hanselaer, Absolute determination of photoluminescence quantum efficiency using an integrating sphere setup, *Rev. Sci. Instrum.*, 2014, **85**(12), 123115.
46 N. M. Bhiri, H. Duim, E. Madirov, J. Nyarige, B. S. Richards and A. Turshatov, Optimizing the short-wavelength infrared photoluminescence quantum yield and brightness of Er^{3+}, Yb^{3+} co-doped yttrium orthophosphate phosphors for tracer-based sorting, *J. Mater. Chem. C*, 2025, **13**(9), 4605–4615.
47 Database of Ionic Radii. https://abulafia.mt.ic.ac.uk/shannon/ptable.php, (accessed 26.06.2026).
48 A. García-Cortés and C. Cascales, Crystal Growth and Optical and Spectroscopic Characterization of the Ytterbium-Doped Laser Molybdate Yb−$Li_3Gd_3Ba_2(MoO_4)_8$, *Chem. Mater.*, 2008, **20**(12), 3884–3891.
49 F. Auzel, Upconversion and Anti-Stokes Processes with f and d Ions in Solids, *Chem. Rev.*, 2004, **104**(1), 139–174.
50 R. Debnath and S. Bose, A comprehensive phononics of phonon assisted energy transfer in the Yb^{3+} aided upconversion luminescence of Tm^{3+} and Ho^{3+} in solids, *J. Lumin.*, 2015, **161**, 103–109.
51 G. Gao, D. Busko, S. Kauffmann-Weiss, A. Turshatov, I. A. Howard and B. S. Richards, Wide-range non-contact fluorescence intensity ratio thermometer based on Yb^{3+}/Nd^{3+} co-doped La_2O_3 microcrystals operating from 290 to 1230 K, *J. Mater. Chem. C*, 2018, **6**(15), 4163–4170.
52 P. Armand, D. Granier, C. Reibel and M. Tillard, Growth, crystal structure, and properties of the $Li_3Ba_2Ln_3(MoO_4)_8$ (Ln = Er, Tm) molybdates, *Solid State Sci.*, 2022, **123**, 106796.
53 R. Balda, J. Fernández, S. García-Revilla and J. M. Fernández-Navarro, Spectroscopy and concentration quenching of the infrared emissions in Tm^{3+} -doped TeO_2-TiO_2-Nb_2O_5 glass, *Opt. Express*, 2007, **15**(11), 6750–6761.
54 R. Balda, J. Fernández, M. A. Arriandiaga, L. M. Lacha and J. M. Fernández-Navarro, Effect of concentration on the infrared emissions of Tm^{3+} ions in lead niobium germanate glasses, *Opt. Mater.*, 2006, **28**(11), 1253–1257.
55 J. R. Lakowicz, *Principles of Fluorescence Spectroscopy*, 3rd edn, Springer, New York, 2006.
56 Y. Zhang, Q. Wang, C. Sun, H. Tian, H. Zhu, X. Yang, H. Wang and H. Liu, Near-infrared luminescence and temperature sensing properties of $Sc_2Mo_3O_{12}$:Nd^{3+}/Yb^{3+}/Ho^{3+} phosphor, *Spectrochim. Acta, Part A*, 2025, **333**, 125869.
57 P. Bhattacharya, *Semiconductor Optoelectronic Devices*, 2nd edn, Prentice Hall, Upper Saddle River, NJ, 1997.